Mon. Not. R. Astron. Soc. **000**, 1–16 (2006) Printed 5 September 2006 (MN LATEX style file v2.2)

A *Subaru/Suprime-Cam* wide-field survey of globular cluster populations around M87 - I: Observation, data analysis, and luminosity function

Naoyuki Tamura[1⋆†], Ray M. Sharples[1], Nobuo Arimoto[2], Masato Onodera[2,3], Kouji Ohta[4], & Yoshihiko Yamada[2]
[1] *Department of Physics, University of Durham, South Road, Durham, DH1 3LE, United Kingdom*
[2] *National Astronomical Observatory of Japan, Mitaka, Tokyo 181-8588, Japan*
[3] *Department of Astronomy, School of Science, University of Tokyo, Tokyo 113-0033, Japan*
[4] *Department of Astronomy, Faculty of Science, Kyoto University, Kyoto 606-8502, Japan*

ABSTRACT

In this paper and a companion paper, we report on a wide-field imaging survey of the globular cluster (GC) populations around M87 carried out with Suprime-Cam on the 8.2m Subaru telescope. Here we describe the observations, data reduction, and data analysis and present luminosity functions of GC populations around M87 and NGC 4552, another luminous Virgo elliptical in our survey field. The imaging data were taken in the B, V, and I bands with a sky coverage of $2^\circ \times 0.^\circ5$ extending from the M87 centre out to ~ 0.5 Mpc. GC candidates were selected by applying a colour criterion on the $B-V$ and $V-I$ diagram to unresolved objects, which greatly reduces contamination. The data from control fields taken with Subaru/Suprime-Cam were also analyzed for subtraction of contamination in the GC sample. These control field data are compatible with those in the M87 field in terms of the filter set (BVI), limiting magnitudes, and image quality, which minimizes the possibility of introducing any systematic errors into the subtractive correction. We investigate GC luminosity functions (GCLFs) at distances $\leqslant 10'$ ($\lesssim 45$ kpc) from the host galaxy centre in detail. By fitting Gaussians to the GCLFs, the V-band turnover magnitude ($V_{\rm TO}$) is estimated to be 23.62 ± 0.06 mag and 23.56 ± 0.20 mag for the GC population in M87 and NGC 4552, respectively. The GCLF is found to be a function of GC colour; $V_{\rm TO}$ of the red GC subpopulation ($V-I > 1.1$) is fainter than that of the blue GC subpopulation ($V-I \leqslant 1.1$) in both M87 and NGC 4552, as expected if the colour differences are primarily due to a metallicity effect and the mass functions of the two subpopulations are similar. The radial dependence of the GCLF is also investigated for the GC population in M87. The GCLF of each subpopulation at $1' \leqslant R \leqslant 5'$ is compared with that at $5' \leqslant R \leqslant 10'$ but no significant trend with distance is found in the shape of the GCLF. We also estimate GC specific frequencies (S_N) for M87 and NGC 4552. The S_N of the M87 GC population is estimated to be 12.5 ± 0.8 within $25'$. The S_N value of the NGC 4552 GC population is estimated to be 5.0 ± 0.6 within $10'$.

Key words: galaxies: elliptical and lenticular, cD — galaxies: star clusters — galaxies: evolution — galaxies: formation — galaxies: individual: NGC 4486, NGC 4552— galaxies: clusters: individual: Virgo cluster.

1 INTRODUCTION

Globular clusters (GCs) are homogeneous stellar systems containing stars with a single age and metallicity, which are in principle simpler to interpret than photometric and spectroscopic observations of the integrated stellar light of a

⋆ E-mail:naoyuki@naoj.org
† Curent address: Subaru Telescope, National Astronomical Observatory of Japan, 650 North A'ohoku Place, Hilo, HI 96720, USA

galaxy. GCs are therefore considered to be powerful probes with which to understand the star formation and chemical enrichment history of their host galaxy. One of the basic findings from observations about GC populations in luminous galaxies is that while thousands of GCs are associated with luminous elliptical galaxies, a significantly smaller number of GCs exist around spiral galaxies with similar luminosities (e.g., Harris 1991; Barmby 2003). This indicates that the specific frequency of GCs (S_N), which is considered to be related to the relative efficiency of GC formation and/or survival compared to galactic halo/bulge stars, depends on galaxy morphology. In fact, S_N has also been suggested to be correlated with local galaxy density, with galaxies in denser environments having larger S_N values (West 1993). The fact that this trend appears to exist even when the sample of galaxies is restricted to ellipticals suggests that GC formation efficiency is more physically linked with galaxy environment. One possibility to explain this observation is biased GC formation in galaxies inhabiting denser environments (West 1993; Blakeslee 1999; McLaughlin 1999). Alternatively, a substantial number of GCs in a luminous galaxy may have an external origin; GCs could be captured from other galaxies through galaxy interactions and accrete onto luminous galaxies in clusters, which would then enhance S_N values as observed.

Recent studies of GCs in the central regions of luminous ellipticals conducted with the *Hubble Space Telescope* (HST) have revealed that many luminous ellipticals have bimodal or multimodal colour distributions of GCs (Gebhardt & Kissler-Patig 1999; Larsen et al. 2001; Brodie et al. 2005). It is found that the mean colours of both red (metal-rich) and blue (metal-poor) GC subpopulations are correlated with the host galaxy luminosities and colours (Larsen et al. 2001; Strader, Brodie & Forbes 2004; Strader et al. 2005; Peng et al. 2006), which will be important constraints on the proposed scenarios for the formation and evolution of GC population such as multiphase collapse scenario (Forbes, Brodie & Grillmair 1997), merger scenario (Ashman & Zepf 1992), hiearchical merging scenario (Beasley et al. 2002), and accretion scenario (Côté, Marzke & West 1998). The small field of view of the HST, however, does not allow one to collect GC populations in the outer halo of a galaxy and investigate their spatial structures, which will also be key pieces of the puzzle (e.g., Moore et al. 2005). Much wider-field studies (e.g., out to $\sim$ 100 kpc from the galaxy centre) of GC populations therefore need to be performed using ground-based data (Rhode & Zepf 2001, 2004; Dirsch et al. 2003; Bassino et al. 2006). Studying GC populations at large distances from the host galaxy is of great importance because the outer halo of the host galaxy, and even the intergalactic space, are presumed to be large reservoirs of blue and metal-poor GCs in the accretion scenario.

In this paper and a companion paper (Tamura et al. 2006; Paper II hereafter), we report a wide-field imaging survey of the GC populations around M87 conducted with Suprime-Cam on the Subaru telescope. Several moderately wide-field studies of GCs surrounding M87 have already been carried out using photometry (Strom et al. 1981; McLaughlin, Harris, & Harris 1994; Harris, Harris, & McLaughrin 1998; Hanes et al. 2001) and spectroscopy (Cohen & Rizhov 1997; Cohen, Blakeslee & Rizhov 1998; Kissler-Patig & Gebhardt 1998; Côté et al. 2001), but all of these studies explored only the regions $\lesssim 10'$ ($\lesssim$ 45 kpc or 5 r_e) from M87. In contrast, the area of our survey is approximately $2^\circ \times 0.^\circ5$ (560 kpc $\times$ 140 kpc) extending from the centre of M87 out to $\sim$ 0.5 Mpc, which is the widest survey yet undertaken of the GC populations in luminous galaxies. In this paper, we focus on describing the observations, data reduction (§ 2) and data analyses such as selection and photometry of GC candidates, incompleteness correction, and subtraction of foreground and background contamination in the GC candidates (§ 3). We derive GC luminosity functions around M87 and NGC 4552, another Virgo luminous elliptical galaxy in our survey field, and estimate the global GC specific frequencies of these luminous ellipticals in § 4. We investigate colour distributions and spatial distributions of GC candidates in Paper II. We adopt distances of 16.1 Mpc (distance modulus of 31.03) to M87, and 15.4 Mpc (distance modulus of 30.93) to NGC 4552, based on measurements using the surface brightness fluctuation method (Tonry et al. 2001). An angular scale of $1'$ corresponds to 4.7 kpc and 4.5 kpc at the distance of M87 and NGC 4552, respectively.

2 OBSERVATIONS, DATA REDUCTIONS, AND CALIBRATIONS

2.1 The M87 Fields

2.1.1 Observations and data reductions

Imaging observations were performed on 17 and 18 March 2004, with Suprime-Cam (SCam) (Miyazaki et al. 2002) on the Subaru telescope. SCam is a mosaic CCD camera with 10 2K×4K CCD chips and the field of view is approximately $34' \times 27'$ on the sky. The pixel scale is $0.''2$ pixel^{-1}. In this observing program, a field of approximately 1 square degree ($136' \times 27'$) extending from M87 towards the east was covered by 4 telescope pointings through B-, V-, and I-band filters. The field IDs and locations are shown in Fig. 1 and the observation log is presented in Table 1. Each field was observed with the telescope dithered by $\sim 5''$. Since this dithering scale is smaller than the gap between the CCDs, the 10 CCD frames are not mosaiced into one continuous frame but are reduced and analyzed individually. A typical exposure time of one frame is 360 sec, 270 sec, and 240 sec in B, V, and I band, respectively; several frames were co-added to give the total exposure times listed in Table 1. On the first night, the sky condition was non-photometric and the transparency was highly variable. On the second night, it was much better but was still hazy with a little variation. We therefore scale the data taken on the first night by shifting the magnitude zeropoints to match with those of the data on the second night, calibrate the reduced data based on the standard stars taken on the second night, and check the calibration using GC photometry in the literature (see next section for details). Typical seeing sizes during the observations were $1.''5$ in B band and $\sim 1.''0$ in V and I bands.

Data reduction was performed with IRAF[1] in a stan-

[1] IRAF is distributed by the National Optical Astronomy Observatories, which is operated by the Association of Universities for Research in Astronomy, Inc. under cooperative agreement with the National Science Foundation.

Field ID	Field centre			Integration time ($m_{\rm lim}$) [sec (mag)]			Seeing size [arcsec]		
(1)	(2)			(3)			(4)		
	α(J2000)	δ(J2000)	b(J2000)	B	V	I	B	V	I
Field 1	$12^h31^m18\overset{s}{.}4$	$12°29'13''$	$74\overset{\circ}{.}6$	3680 (25.6)	1350 (25.1)	3480 (24.6)	1.8	1.0	1.0
Field 2	$12^h33^m42\overset{s}{.}8$	$12°27'37''$	$74\overset{\circ}{.}8$	2640 (25.9)	1350 (25.2)	3690 (24.7)	1.2	1.0	1.0
Field 3	$12^h36^m08\overset{s}{.}8$	$12°24'35''$	$74\overset{\circ}{.}9$	1800 (25.7)	1350 (25.2)	2640 (24.5)	1.5	1.0	1.1
Field 4	$12^h38^m33\overset{s}{.}2$	$12°24'35''$	$75\overset{\circ}{.}0$	2280 (26.1)	1350 (25.2)	4380 (24.8)	1.1	1.0	1.0
HDF-N	$12^h36^m46\overset{s}{.}7$	$62°11'50''$	$54\overset{\circ}{.}8$	6000 (26.6)	4800 (25.5)	4200 (25.2)	0.8	1.1	0.9
Lockman Hole	$10^h35^m55\overset{s}{.}2$	$57°42'18''$	$51\overset{\circ}{.}3$	6000 (26.9)	4800 (26.0)	3600 (24.8)	1.0	1.1	1.3

Table 1. Observation log. Data for HDF-N and Lockman Hole are retrieved from SMOKA. Col. (3): The integration times were calculated including data taken under non-photometric conditions on the first night (hence the interpretation is not straightforward). Number in the parentheses indicates 50 % completeness to point sources estimated with artificial star test. Col. (4): The seeing sizes are estimated in the stacked images.

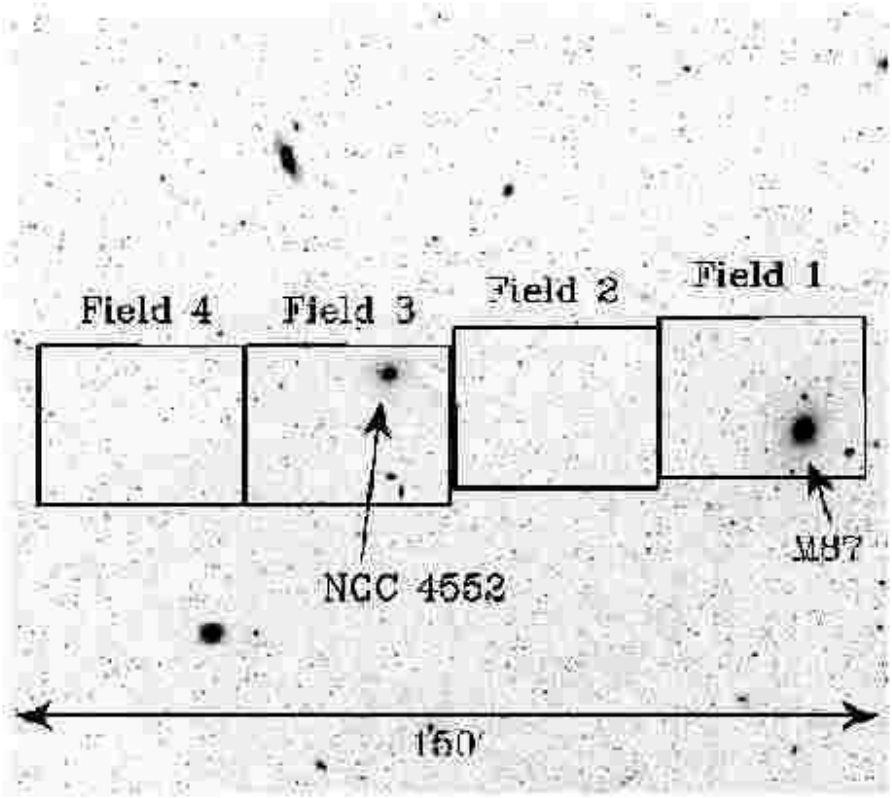

Figure 1. Locations and IDs of the observed fields. Each box indicates one SCam field of view. The background is a DSS image. North is up and East is left.

dard manner; bias subtraction, flat-fielding, masking bad columns and saturated pixels, sky subtraction, registration, and average stacking with a 3 σ clipping algorithm. Sky subtraction was performed by employing the following two steps. Firstly, an image was divided into a mesh of 128 $\times$ 128 pixels ($\sim 26'' \times 26''$) and a median sky value was estimated in each window after bright objects were masked. A sky value in each pixel was then estimated by an interpolation of the median sky values for the adjacent windows. A background image of an object frame was created with this process which was then subtracted. For CCD frames where bright galaxies or their envelopes are quite extended (e.g., near M87 and NGC 4552), this method cannot be applied. Instead, an average background was estimated as a single value using a "blank" CCD frame within the same exposure. It was corrected for the sensitivity difference between the two CCD frames using the flat-field frames. In stacking CCD frames, aperture photometry of $20 - 30$ bright stellar objects selected using SExtractor (Bertin & Arnout 1996) based on the `CLASS_STAR` index was performed in each frame and the zeropoint of the frame was shifted so as to match that in a frame taken on the second night. PSF matching

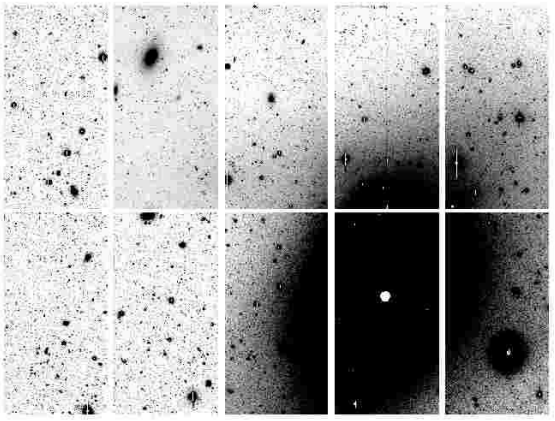

Figure 2. Reduced data for Field 1 (V band). North is up and East is left.

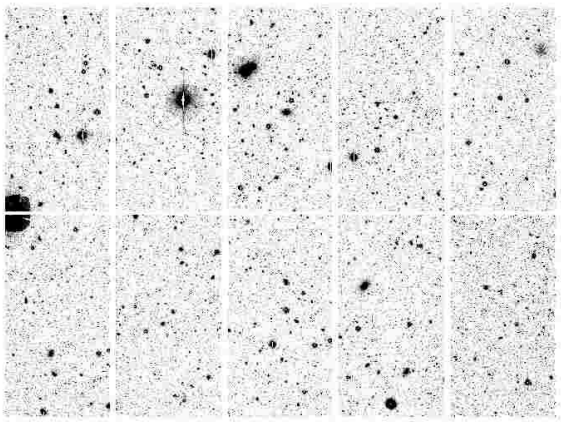

Figure 3. Same as Fig. 2, but for Field 2.

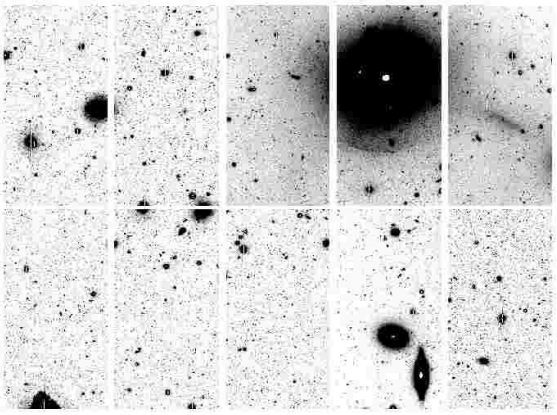

Figure 4. Same as Fig. 2, but for Field 3.

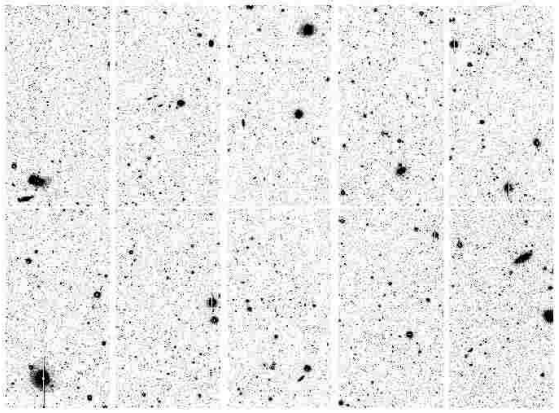

Figure 5. Same as Fig. 2, but for Field 4.

was not performed to avoid degradation of image quality. The stacked images are presented in Fig. 2 − 5.

2.1.2 Photometric and astrometric calibration

Photometric calibration of the M87 fields was performed using standard stars from Landolt (1992) which were observed at the beginning and end of the second night. Several standard stars were imaged on each CCD chip so that the calibration could be carried out individually. Photometry of standard stars was performed within a $12''$ diameter aperture. After excluding saturated stars and those in crowded regions, magnitude zeropoints and the trends with sec z and colours were calculated. The estimated accuracy in the fitting procedure is $0.03 - 0.05$ mag.

Since our data include frames which were taken under non-photometric sky conditions, we check the photometric calibration by comparing our photometry of GCs around M87 with that in the literature. We make use of GC photometry in the V and I bands by Harris, Harris, & McLaughlin (1998, HHM hereafter) and that in the Washington system (C and T_1) by Hanes et al. (2001, H01 hereafter). The GC photometry by H01 is converted to the standard BVI system by using the formulae obtained by Geisler (1996). PSF-fitting photometry was carried out for GCs using the PSF and ALLSTAR tasks in the DAOPHOT package of IRAF. A PSF was determined using ~ 20 moderately bright (unsaturated) stellar objects in each CCD frame, which were selected using SExtractor based on the `CLASS_STAR` index. The PSF obtained was also used for GC photometry, since the GCs at the distance of the Virgo cluster are unresolved at the seeing sizes of our images. Galactic extinction was then corrected using reddening maps from Schlegel, Finkbeiner, & Davis (1998). We are primarily concerned about zeropoint offsets for V-band magnitude and $B-V$ and $V-I$ colours; the V band image is used as a selection band to make a catalog of GCs and $B-V$ and $V-I$ colours are used to isolate GC candidates from other unresolved objects (see § 3.3 for details). While $C-T_1$ can be converted into $B-V$ with a small error, it is not converted to $V-I$ with a good accuracy (Geisler 1996). We therefore decided to estimate the zeropoint offset in $B-V$ from the comparison with H01 and those in V and $V-I$ from the comparison with HHM. Our GC photometry is compared with that from H01 and HHM in Fig. 6. Dotted lines in these plots indicate the approximate edges of the colour range which is expected to be occupied by GCs. These comparisons suggest that there are some zeropoint offsets between our photometry and that in the literature. The zeropoint offsets in V, $B-V$ and $V-I$

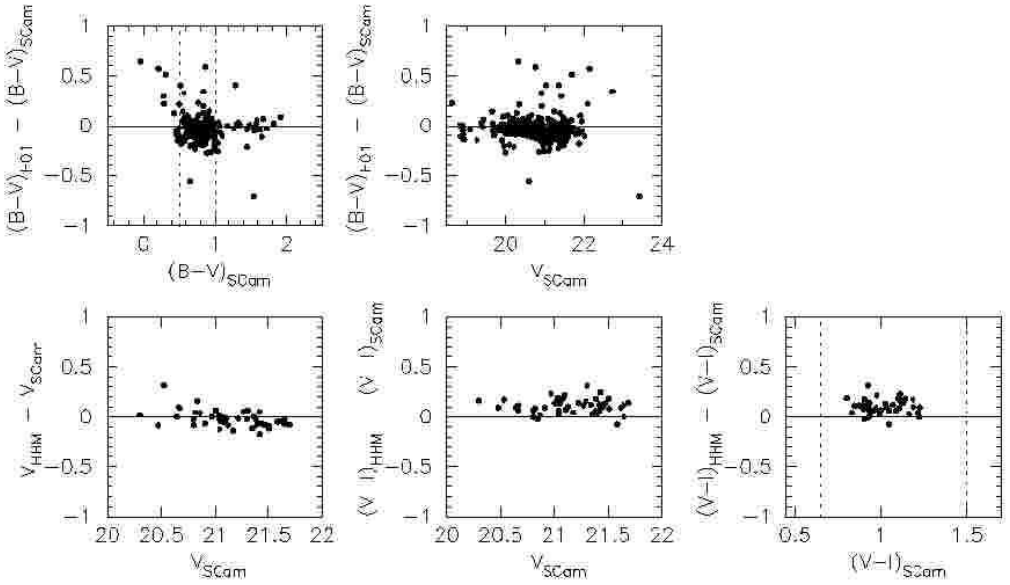

Figure 6. Comparison of our photometry ($V_{\rm SCam}$, $(B-V)_{\rm SCam}$, and $(V-I)_{\rm SCam}$) with that by H01 ($(B-V)_{\rm H01}$) and HHM ($V_{\rm HHM}$ and $(V-I)_{\rm HHM}$). Dotted lines in the plots for the colours approximately show reddest and bluest boundaries expected for GCs.

are 0.04 mag, 0.05 mag and 0.10 mag, respectively. Our magnitude and colours are corrected for these zeropoint offsets in the following analyses.

We performed astrometric calibration against the 2MASS catalog using the CCMAP task in IRAF. A plate solution (second order polynomial with full cross terms) was computed for each CCD chip using stars with $J \leqslant 17$ mag. The fitting accuracy is typically $\sim 0\farcs2$.

2.2 The Control Fields

In addition to the M87 field data, we also analyze BVI images of the (blank) fields, HDF-N and Lockman Hole (LH), retrieved from the Subaru-Mitaka-Okayama-Kiso Archive (SMOKA) system (Baba et al. 2002). These data were taken with SCam on the Subaru telescope during several observing runs in 2001: 23 and 24 Feb for BVI on HDF-N and B on LH, and 22 and 23 Apr for V and I on LH (Capak et al. 2004). This information is also summarized in Table 1. These control field data are used to estimate contamination in the sample of GC candidates and to statistically subtract it, which is essential for investigating properties of GC populations such as the luminosity function and colour distribution. We emphasize that these control fields are also at high galactic latitudes (Table 1), and that the data cover reasonably wide sky areas (one SCam field of view: ~ 900 arcmin^2) and are comparable with our data in the M87 field in terms of the filter set, limiting magnitudes, and image quality. This minimizes the possibility of introducing any systematic errors into the subtractive corrections for foreground and background contamination in the GC sample.

The data reduction was carried out with SDFRED (Yagi et al. 2002; Ouchi et al. 2004), which is a reduction pipeline optimized for SCam data of blank fields. The basic reduction procedure is the same as that applied to the M87 field data. The large scale of telescope dithering ($\sim 1'$) for these control field data enables the CCD frames to be stacked into one continuous image with sensitivity differences between CCDs corrected by using stellar objects in the overlap regions. To avoid any complications due to a possible drop of limiting magnitude near the field edge, we use only the central $27' \times 27'$ region in the following analyses. The magnitude zeropoints of the HDF-N data were calculated using the photometry catalog by Capak et al. (2004). These authors did not observe any standard stars during the observations and determined magnitude zeropoints by exploiting the accurate photometry of objects in the region where deep HST/WFPC2 data are available. The best-fit SEDs to the multi-band photometry of the objects (Fernández-Soto, Lanzetta & Yahil 1999) were used to account for the slight differences in the filter responses between Subaru/SCam and HST/WFPC2. Since the B band data of the LH field were taken in the same runs as for the HDF-N, the same zeropoint is adopted. The V and I band data of the LH field were taken on different observing runs and standard stars were observed at elevations similar to those of the LH field during the night. Magnitude zeropoints were derived from these data. Galactic extinction was then corrected using Schlegel et al. (1998).

3 DATA ANALYSES

3.1 Halo Light Subtraction

As shown in Figs. 2 and 4, M87 and NGC 4552 extend across several CCD frames and their halos have to be subtracted to reveal the GC populations. We removed the halos by conducting an iterative median smoothing and subtraction (e.g., McLaughlin, Harris, & Hanes 1994). First, we subtract unresolved objects from an image. This process is not mandatory, but it helps better model the extended halo light distributions or their residuals in subsequent iterations.

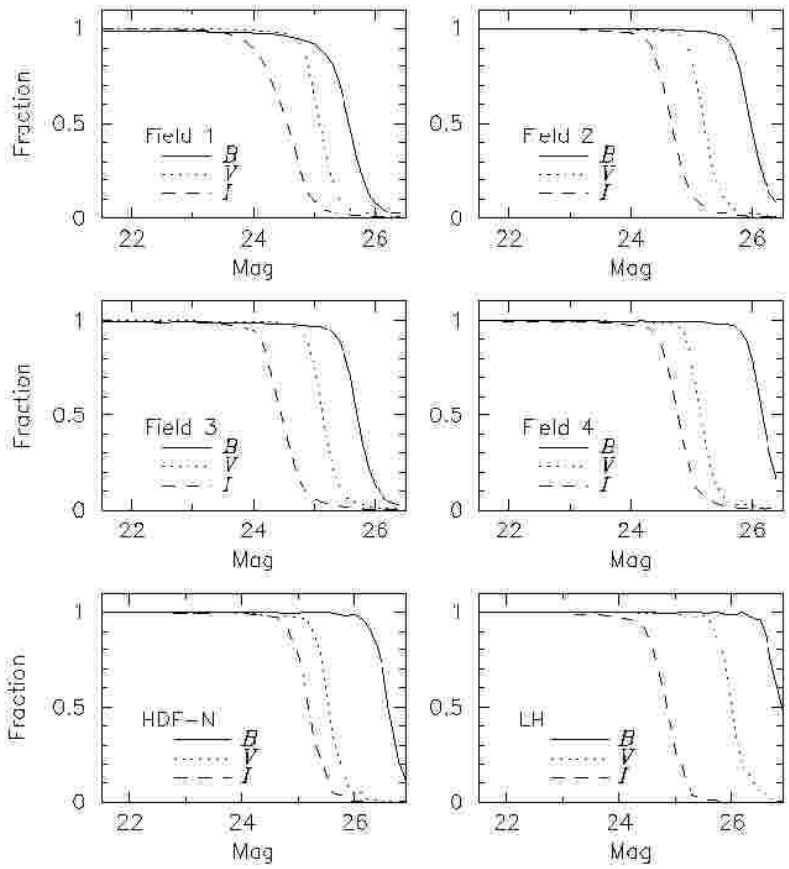

Figure 7. Overall detection completenesses in BVI bands are overplotted. Top and middle panels: the results in the M87 fields are shown. Bottom panels: those in the control fields are indicated.

Object detection was performed with SExtractor and unresolved objects were picked out based on the `CLASS_STAR` index. A PSF was determined using moderately bright stars, which was then fitted to unresolved objects and the fitted profiles were subtracted from the original image using the ALLSTAR task. The resulting image was median-smoothed to create an image with a halo light distribution which was subtracted from the original image. This procedure was repeated 4 times with the mesh size successively reduced (128, 64, 32, and 32 pixels).

3.2 Artificial Star Tests

We performed artificial star tests for investigating detection completeness to point sources on the B-, V-, and I-band images, after bright galaxies were subtracted if necessary. Using the IRAF STARLIST and MKOBJECT tasks, artificial stars with the same PSF as that determined using real unresolved objects were distributed on the original image. For a series of tests, 500 artificial stars within a certain range of magnitude $[m, m+0.5$ mag] were generated while successively changing the magnitude range as the test progressed. SExtractor was then used for object detection and the fraction of artificial stars detected (i.e., detection completeness) was calculated as a function of magnitude. Note that faint stars could be rejected by DAOPHOT even if they are detected by SExtractor, but the fraction of such artificial stars turns out to be small ($\leqslant 1$ %) throughout the magnitude range investigated in our artificial star tests. We performed these artificial star tests on all the CCD frames in all the observed fields (Field $1-4$) and the overall completeness in each observing field is plotted against B-, V-, and I-band magnitude in the top and middle panels of Fig. 7. This indicates the presence of a slight field-to-field variation in limiting magnitude. The detection completeness is also a function of galactocentric distance; for instance, limiting magnitudes are ~ 0.5 mag brighter near the centre of M87 where the noise is higher. Therefore, when investigating the luminosity function and colour distribution of GC candidates within an annulus at a certain distance from the host galaxy, we correct for incompleteness using the completeness functions estimated within the same annulus. Especially near the luminous ellipticals, we divide the annulus into sub-annuli to follow the local variation of the incompleteness in the annulus. The artificial star tests were also executed on the control field images and the overall completeness functions are indicated in the bottom panels of Fig. 7. The magnitudes giving 50 % completeness on the M87 fields and the control fields are listed in Table 1.

Since unresolved objects are firstly selected based on the `CLASS_STAR` indices on the V-band image when selecting GC candidates (see § 3.3), one also needs to consider biases asso-

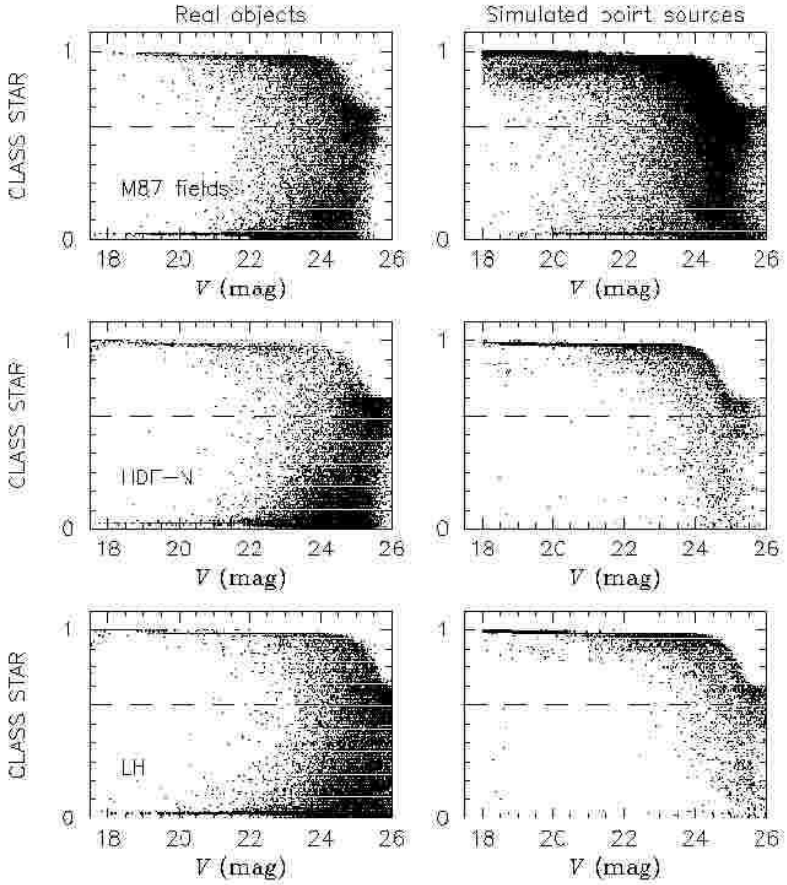

Figure 8. `CLASS_STAR` indices of detected objects in the V band images of the M87 fields, HDF-N field, and LH field are plotted against their magnitudes in the top, middle, and bottom panels, respectively. Dashed line indicates the lower limit for selection of unresolved objects (0.6).

ciated with the selection of unresolved objects in addition to the simple detection incompleteness as mentioned above. In the top panels of Fig. 8, `CLASS_STAR` indices of the detected objects (left panel) and the artificial stars (right panel) in the M87 fields are plotted against V-band magnitude. In the middle and bottom panels, the results in the control fields are shown. These plots indicate that the `CLASS_STAR` index of a point source tends to be underestimated at fainter magnitudes and more stellar objects are expected to be excluded when we classify objects with `CLASS_STAR` indices larger than a certain value as unresolved. We quantify this selection effect as functions of V magnitude and distance from the host galaxy based on these artificial star tests.

3.3 Selection and Photometry of GC Candidates

We begin selection of GC candidates with object detection using SExtractor. Firstly, we picked out all objects having at least 20 connected pixels (~ 0.8 arcsec^2, which is approximately equal to the FWHM area of the PSF) more than 2 σ above the local background (only objects selected in all the three B-, V-, and I-bands were used for analysis). Secondly, we selected objects with `CLASS_STAR` indices larger than 0.6 as unresolved objects. The V-band image was used for this classification because it has the best image quality in our data. The subsequent results do not change if this cutoff for the `CLASS_STAR` index is set to 0.5 or 0.7. We note that our criterion (`CLASS_STAR` $\geqslant 0.6$) is more stringent than those adopted in previous GC studies ($\geqslant 0.4$ in Dirsch et al. 2003 and $\geqslant 0.35$ in Forbes et al. 2004) using data with better image quality than our data.

PSF-fitting photometry was performed for these unresolved objects and their B, V, and I magnitudes were measured. In this process, a residual sky background around an object is estimated within an annulus $10''$ away from the object with a $4''$ width and is subtracted. Errors in the V-band magnitude and $B-V$ and $V-I$ colours due to a PSF fitting error and sky subtraction error are plotted as a function of V-band magnitude in the top, middle, and bottom panels of Fig. 9 for unresolved objects in the M87 fields, HDF-N field, and LH field, respectively. A colour criterion was then imposed on these unresolved objects to isolate GC candidates. We show this colour criterion as the shaded region in Fig. 10 which includes almost all the Galactic GCs in the catalog by Harris (1996)[2] but minimizes the contamination by foreground stars and background galaxies. The $B-V$ and $V-I$ colour-colour diagrams of the unresolved objects on our im-

[2] The catalog used here is the version last updated in 2003.

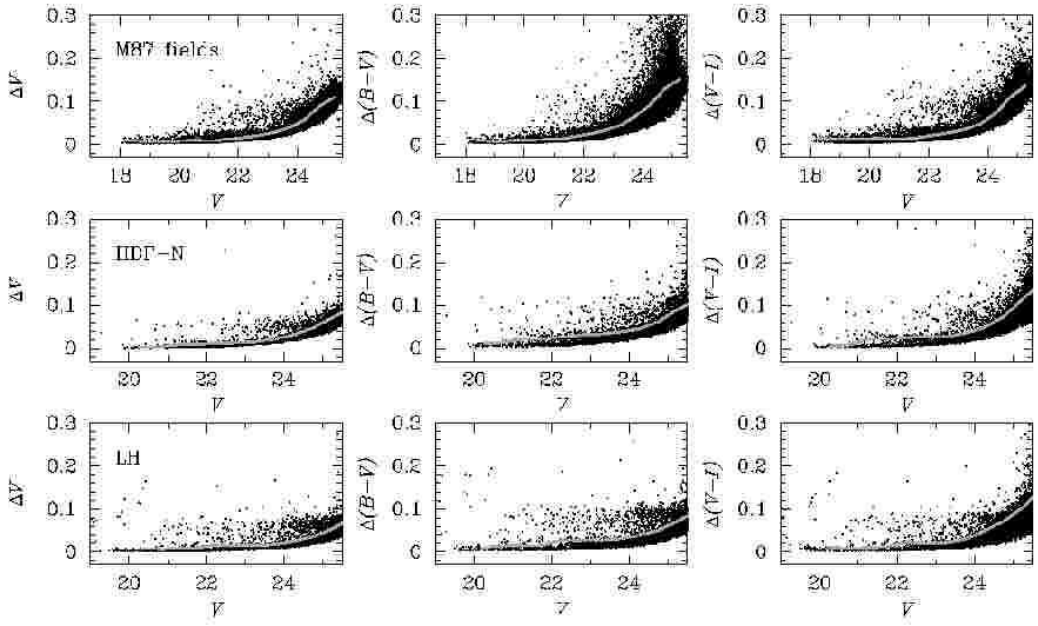

Figure 9. For the unresolved objects, errors of V-band magnitude (left), $B-V$ colour (centre) and $V-I$ colour (right) from the PSF-fitting photometry are plotted as a function of V-band magnitude. Grey line indicates the boundary below which 80 % of the unresolved objects are included at a given magnitude. In the top, middle, and bottom panels, the results in the M87 fields, HDF-N field, and LH field are shown, respectively.

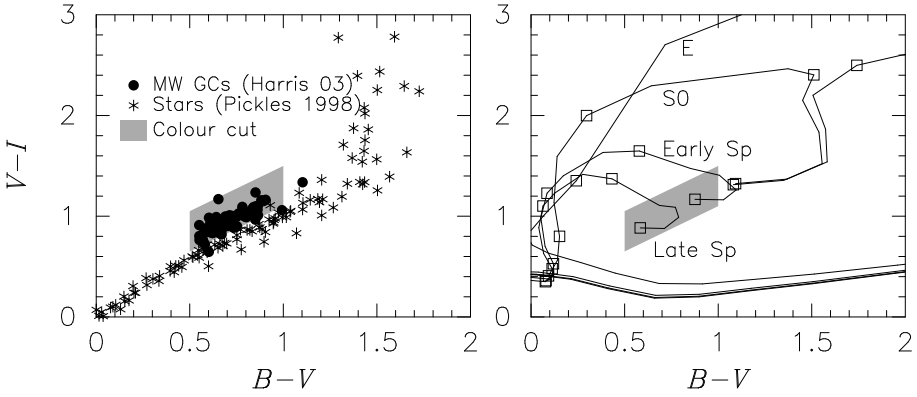

Figure 10. The colour criterion to select GC candidates is indicated by a shaded region. In the left panel, colours of Galactic GCs in the catalog by Harris (2003 version) are plotted with circles, and stellar colours based on a stellar flux library by Pickles (1998) are plotted with asterisks. Galactic extinctions for the GC colours are corrected using the colour excess of each GC in the catalog. In the right panel, evolutionary tracks of the galaxy colours calculated using PEGASE v2.0 (Fioc & Rocca-Volmerange 1997) are indicated. Open squares are plotted at redshifts of 0, 0.5, 1.0, 1.5, and 2.0 on each track. Note that the galaxy colours at $z = 0$ are plotted around the middle of this panel and go towards outer regions at higher redshifts.

ages are indicated in Fig. 11; the objects are divided into panels based on their distances from M87, apart from those in the HDF-N field, which are plotted in the bottom right panel for reference. Black dots indicate unresolved objects which pass the colour selection, while grey dots are those which do not satisfy the colour criterion. Some unresolved objects sitting outside the colour criterion are accepted as GC candidates by taking into account errors in the colours (e.g., Rhode & Zepf 2001); if colours of unresolved objects can satisfy the colour criterion within their errors, they are sampled as GC candidates. This "inclusive" colour selection allows us to incorporate fainter GCs which are more likely to be scattered out of the colour criterion due to larger errors in the colours. Although contaminating objects may also be included, they are expected to be corrected for by the control field data (see § 3.4).

3.4 Correction of Incompleteness and Foreground and Background Contamination

In deriving a GC luminosity function (GCLF) and colour distribution, incompleteness correction is undertaken as follows. The number of GC candidates at a certain V magnitude is firstly corrected for the incompleteness in detection

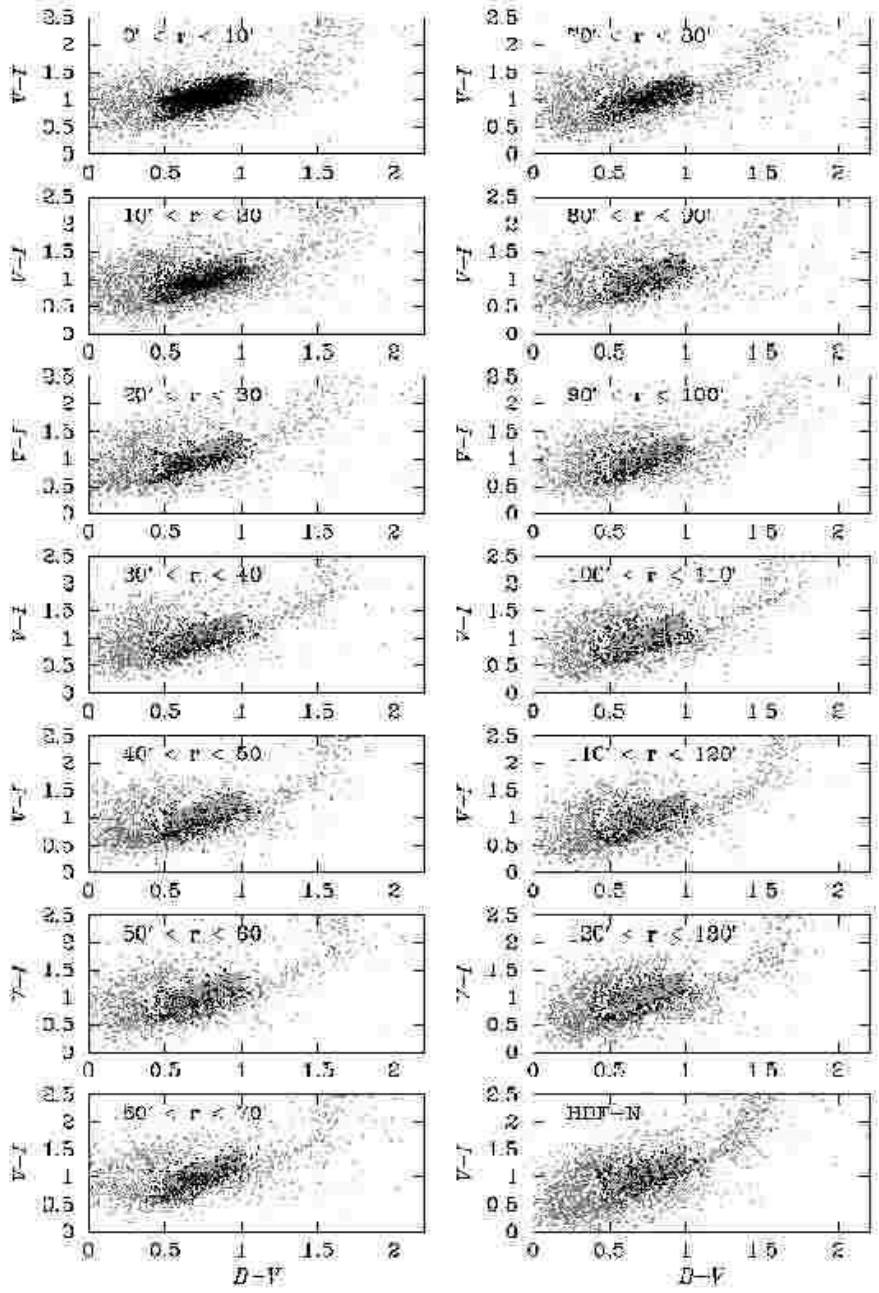

Figure 11. $B-V$ and $V-I$ colour-colour diagrams for the unresolved objects. The data in the M87 fields are divided into panels based on the distances of the sources from M87. In the bottom right panel, the unresolved objects in the HDF-N data (see § 2.2) are plotted. Black dots indicate unresolved objects which pass the colour cut, and grey dots are those which do not. The shaded region in each panel indicates the colour criterion. Some objects sitting outside the colour criterion are accepted because we take into account errors in both of the colours in applying the colour cut to these objects (see text for details).

and selection of unresolved objects on the V-band image. Detection incompleteness on the B and I band images is then corrected; GCs with a given V-band magnitude are divided into bins according to their $B-V$ and $V-I$ colours, and the numbers of objects are multiplied by a factor to correct for the incompleteness at the B and I magnitudes ($B=(B-V)+V$, $I=V-(V-I)$). These incompleteness corrections are also applied to GC candidates found in the control fields.

Although the selection using the two colour diagram is expected to efficiently isolate GCs from foreground stars and background unresolved galaxies, there are still likely to be some contaminating objects, and a subtractive correction of this contamination is essential to investigate GC properties in the outer halo of the host galaxy where the GC surface number density is very low. We extract contaminating populations of unresolved objects from the control fields by using selection criteria identical to those adopted in the M87

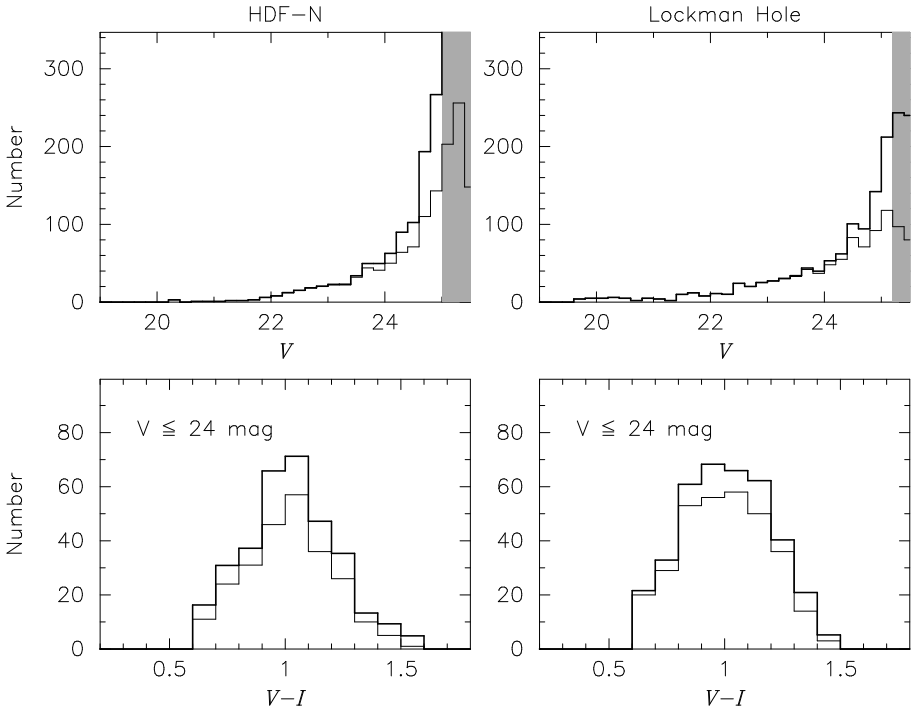

Figure 12. *Upper panels*: Luminosity functions of the unresolved objects which pass the colour selection in the HDF-N (*left*) and the LH (*right*). Thin line shows raw LF and thick line indicates incompleteness-corrected LF. Shaded region at the right hand side corresponds to the magnitude range where the completeness is lower than 50 %. *Lower panels*: Colour distributions of the unresolved objects ($V \leqslant 24$ mag) which pass the colour selection. Thin line shows raw distribution and thick line indicates incompleteness-corrected distribution.

fields; objects with `CLASS_STAR` $\geqslant 0.6$ are selected as unresolved objects and GC candidates are isolated by using the same colour criterion on the $B-V$ vs. $V-I$ colour-colour diagram.

When subtracting contamination in a certain region within the M87 survey field, we take into account differences in data quality, especially errors in the colours at a certain V magnitude, between the M87 field and control field. Since the errors in the control fields are smaller than those in the M87 field, a smaller number of objects would be scattered into the colour criterion in the control fields and the contamination could be underestimated. We pick out unresolved objects within narrow ranges (± 0.1 mag) of V, $B-V$ and $V-I$ from both the M87 field and control field and calculate the differences of typical errors in the colours between the two samples of unresolved objects. We then randomize the measured colours of the unresolved objects in the control field by an amount which is determined from a Gaussian distribution whose average is zero and whose standard deviation is estimated from the difference of the typical errors in the colours. The observational errors in the colours of the unresolved objects in the control field are therefore replaced with the typical errors of those in the M87 field. This sequence is repeated in the control field for different V magnitudes and the colours successively changed, which provides a mock catalog of unresolved objects in the control field whose error characteristics are compatible with those in the M87 field. Based on the colours and errors in this mock catalog, the colour selection is performed to pick up contaminating objects in the control field[3]. The luminosity function and colour distribution of these contaminating objects including the incompleteness corrections are then subtracted from those in the M87 field with the survey area normalized.

In Fig. 12, the V-band luminosity functions and $V-I$ colour distributions of GC candidates found in the control fields are displayed. Note that these are obtained by considering the entire region of the M87 survey field. The LF and colour distribution in the control fields are normalized to the survey area of a target field when subtracted. Most of these contaminating objects are likely to be background galaxies with compact morphology; candidates are dwarf ellipticals and blue compact dwarfs, the latter of which need to be at higher redshifts than the former to meet the colour criterion. Foreground stars can also be scattered into the GC colour selection due mainly to photometric errors, but since the errors in the colours are ~ 0.1 mag even at $V \sim 24.5$ mag, which is approximately the faintest magnitude of GCs studied in this work, their contribution is presumed to be smaller than the background galaxies.

[3] Because this sequence involves random numbers, the GC candidates in a control field needs to be defined by a number of attempts based on the Monte Carlo technique. But in fact, the variance of the average population is small because the "inclusive" selection of GC candidates does not give a sharp cutoff on the $B-V$ and $V-I$ colour-colour diagram.

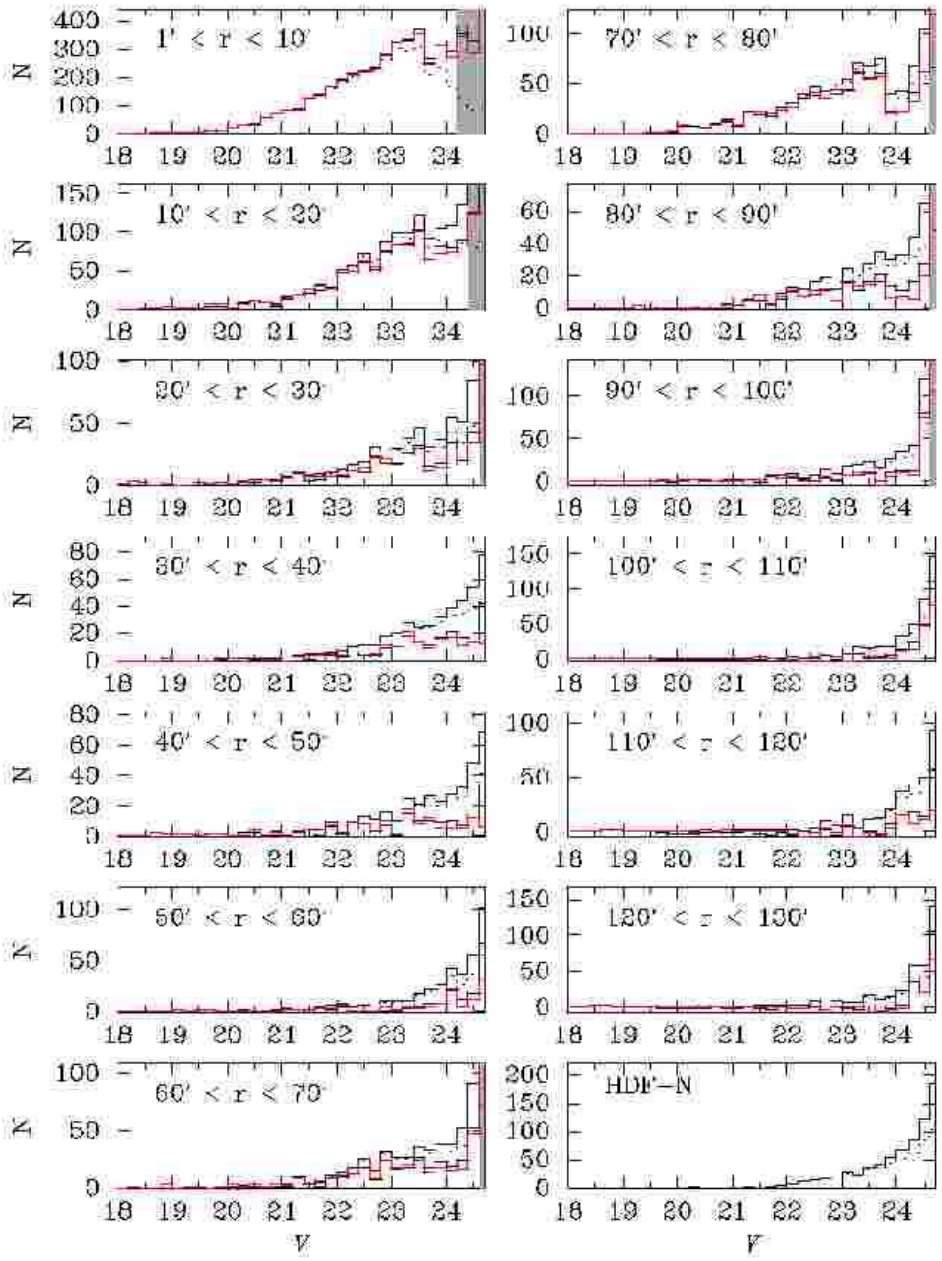

Figure 13. GC Luminosity Functions (GCLFs) obtained within annuli centered on M87 are indicated. The dotted line indicates a raw LF (without incompleteness correction or control field subtraction) and thin black line describes an LF after the incompleteness is corrected (but no field subtraction is performed yet). The red line and the thick black line are those where the control field subtraction is performed after the incompleteness correction: red (black) line shows the LF where the control field subtraction is performed using the HDF-N (LH) data, respectively. The shaded region indicates the magnitude range where the completeness is lower than 50 %. In the bottom right panel, the LF of unresolved and colour-selected contaminating objects in the HDF-N field is shown for reference (survey area is not normalized).

4 RESULTS AND DISCUSSIONS

4.1 Globular Cluster Luminosity Function

In Fig. 13, GCLFs obtained within annuli centered on M87 are presented. The dotted lines indicate raw GCLFs without incompleteness correction or control field subtraction, and the thin black lines show GCLFs after the incompleteness is corrected for (but no subtractive correction for contamination is performed yet). The red (thick black) lines show GCLFs after the control field subtraction is also performed based on the HDF-N (LH) field, respectively. In Fig. 14, the GCLFs after the incompleteness correction and field subtraction using the HDF-N data are divided into red ($V - I > 1.1$) and blue ($V - I \leqslant 1.1$) GC subpopulations. The black line shows the GCLF for the total GC population (blue + red). The boundary colour of the blue and red GCs

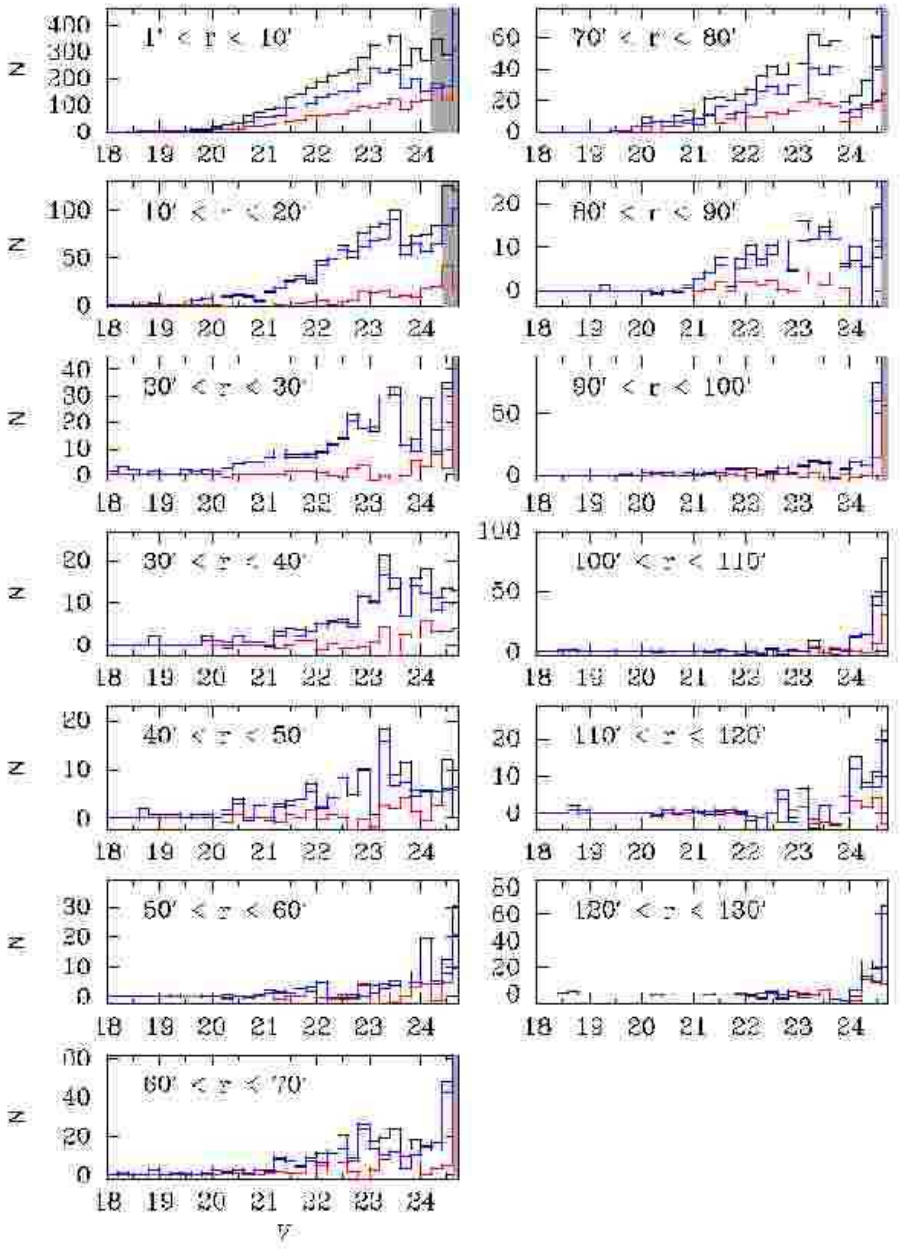

Figure 14. Black line indicates GCLF after the incompleteness is corrected and the control field is subtracted using the HDF-N data (same as that described with the red line in Fig. 13). This is divided into two LFs depending on GC colour: Red and blue lines indicate the LFs for red ($V - I > 1.1$) and blue ($V - I \leqslant 1.1$) GC candidates, respectively.

corresponds approximately to the middle of the peak colours in the bimodal colour distributions (see Paper II). Note that there is a local maximum of GC number in the $70' < r < 80'$ bin due to the GC population of NGC 4552 at a distance of $\sim 75'$ from M87. GCLFs in the outermost regions tend to have some negative bins due to the field subtraction. In both of these figures, the shaded region indicates the magnitude range where the completeness is lower than 50 %. Note that the completeness is calculated by considering not only the simple detection completeness on the V band image but also the selection efficiency of unresolved objects based on the `CLASS_STAR` index and the completeness in B and I bands at the corresponding magnitudes depending on the GC colours. We investigate and discuss the spatial distributions of GC populations in detail in Paper II.

A Gaussian fitted to the GCLF obtained using only GCs at distances smaller than $10'$ ($\sim$ 45 kpc) from the host galaxy is plotted in Fig. 15 (we fit a Gaussian to the binned data). The fainter part of the GCLF in the shaded region where the completeness is lower than 50 % is not used in this fitting process. The turnover magnitude ($V_{\rm TO}$) and dispersion (σ) of the GCLF are then estimated to be $V_{\rm TO} = 23.62 \pm 0.06$ mag and $\sigma = 1.50 \pm 0.04$ mag for the GC population in M87. For the NGC 4552 GCs,

Galaxy		All GCs		Red GCs		Blue GCs	
		$V_{\rm TO}$ (mag)	σ (mag)	$V_{\rm TO}$ (mag)	σ (mag)	$V_{\rm TO}$ (mag)	σ (mag)
M87	$(1' \leqslant R \leqslant 10')$	23.62 ± 0.06	1.50 ± 0.04	23.85 ± 0.19	1.57 ± 0.09	23.35 ± 0.05	1.38 ± 0.04
M87	$(1' \leqslant R \leqslant 5')$	23.63 ± 0.08	1.48 ± 0.05	23.77 ± 0.23	1.54 ± 0.11	23.36 ± 0.11	1.44 ± 0.05
M87	$(5' \leqslant R \leqslant 10')$	23.52 ± 0.08	1.44 ± 0.05	23.97 ± 0.43	1.48 ± 0.22	23.37 ± 0.08	1.36 ± 0.05
M87	$(R \lesssim 1'$; K99)	23.67 ± 0.07	1.39 ± 0.06	–	–	–	–
M87	$(R \lesssim 1'$; L01)	$23.44^{+0.04}_{-0.08}$	–	$23.52^{+0.06}_{-0.08}$	–	$23.30^{+0.06}_{-0.12}$	–
NGC 4552	$(1' \leqslant R \leqslant 10')$	23.56 ± 0.20	1.34 ± 0.12	23.75 ± 0.35	1.40 ± 0.18	23.33 ± 0.16	1.09 ± 0.10
NGC 4552	$(1' \leqslant R \leqslant 5')$	23.48 ± 0.22	1.42 ± 0.14	23.85 ± 0.44	1.59 ± 0.24	23.52 ± 0.28	1.31 ± 0.18
NGC 4552	$(R \lesssim 1'$; KW01)	23.54 ± 0.18	1.3 (fixed)	–	–	–	–
NGC 4552	$(R \lesssim 1'$; L01)	$23.19^{+0.11}_{-0.15}$	–	$23.52^{+0.22}_{-0.20}$	–	$22.91^{+0.15}_{-0.18}$	–

Table 2. Parameters of Gaussians fitted to GCLFs. In the outer region of NGC 4552, no Gaussian fits were attempted due to the poor statistics. The GCLF parameters in the core region ($R \lesssim 1'$) of M87 and NGC 4552 taken from the literature are also shown for comparison: Kundu et al. (1999; K99), Kundu & Whitmore (2001; KW01), and Larsen et al. (2001; L01). L01 fitted t_5 functions to the GCLFs and hence we only indicate the $V_{\rm TO}$s.

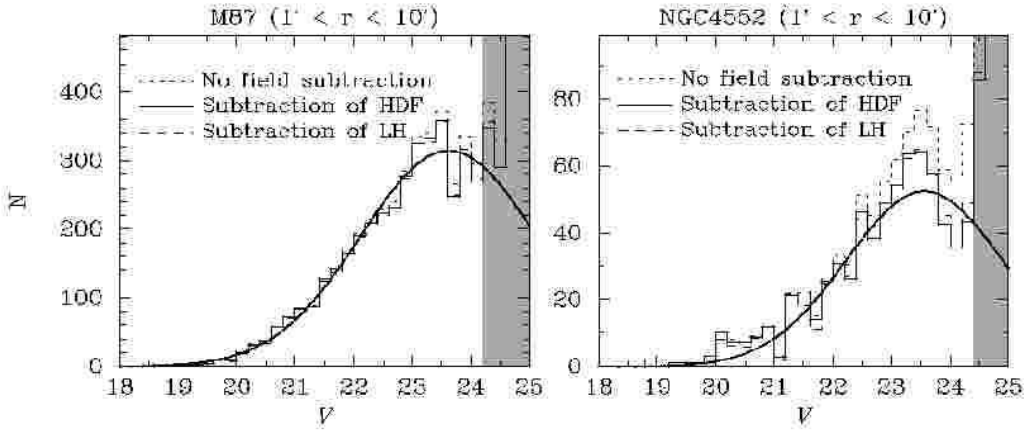

Figure 15. Histograms show GCLFs obtained only using GCs at distances $\leqslant 10'$ from host galaxy centre. Dotted line indicates incompleteness-corrected GCLF. Solid and dashed lines show GCLFs after subtracting control field populations based on the HDF-N and LH data, respectively. A Gaussian fitted to the GCLF is overplotted by a solid line. Shaded region indicates the magnitude range where the completeness is lower than 50 %.

$V_{\rm TO} = 23.56 \pm 0.20$ and $\sigma = 1.34 \pm 0.12$ mag. In Fig. 16, the GCLFs of the red and blue GC subpopulations are shown with fitted Gaussians. Again the shaded region indicates the magnitude range where the completeness calculated by using all the GCs (i.e., blue + red) is lower than 50 %. This limiting magnitude does not change a lot if only the red or blue GC subpopulation is considered since our B- and I-band images are deep enough not to miss a significant number of red or blue globular clusters detected on the V-band image. The fitted Gaussians suggest that the GCLF depends on subpopulation; the $V_{\rm TO}$ of the red GC subpopulation is ~ 0.5 mag and 0.4 mag fainter than that of the blue one for M87 and NGC 4552, respectively, although the results for the NGC 4552 GCs are less significant due to the large errors. Larsen et al. (2001) present similar results using the HST/WFPC2 data, although their $V_{\rm TO}$ values tend to be brighter than those from other studies. This difference of $V_{\rm TO}$ between the GC subpopulations is perhaps because of a metallicity difference (Ashman, Conti & Zepf 1995; Elson & Santiago 1996; Jordán et al. 2002). $V_{\rm TO}$ and σ of the GCLFs are summarized in Table 2.

The GCs within $10'$ of M87 are further divided into two samples at a boundary of $5'$ and the GCLFs of all GCs, red GCs, and blue GCs in the inner and outer regions are presented in Fig. 17. Gaussians are also fitted to these GCLFs and the $V_{\rm TO}$ and σ are summarized in Table 2. This indicates that the shape of GCLF is not significantly different between the inner region ($1' \leqslant R \leqslant 5'$) and the outer region ($5' \leqslant R \leqslant 10'$) for red GCs or blue GCs. Furthermore, the GCLF shape for all GCs is consistent with that in the core region ($\leqslant 1'$) obtained by Kundu et al. (1999) using HST/WFPC2: $V_{\rm TO} = 23.67 \pm 0.07$ mag ($\sigma = 1.39 \pm 0.06$). This suggests that the GCLF shape of the M87 GCs is not a strong function of distance from the host galaxy. We note that the fainter part of the GCLF for all GCs tends to be more deficient at the larger distance; this is due to the lower contribution of the red GC subpopulation in the outer region. Any radial dependence of the GCLF is unclear for the GC population around NGC 4552 because the number of

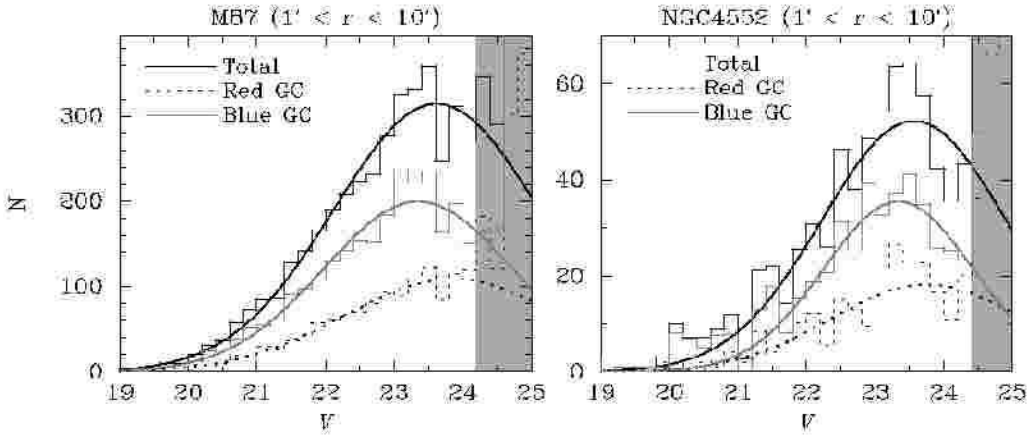

Figure 16. The GCLF of all GCs, red GCs, and blue GCs is indicated by a black solid line, dotted line, and grey solid line, respectively. Incompleteness was corrected and contamination was subtracted based on the HDF-N data. Gaussians fitted to the GCLFs are also plotted.

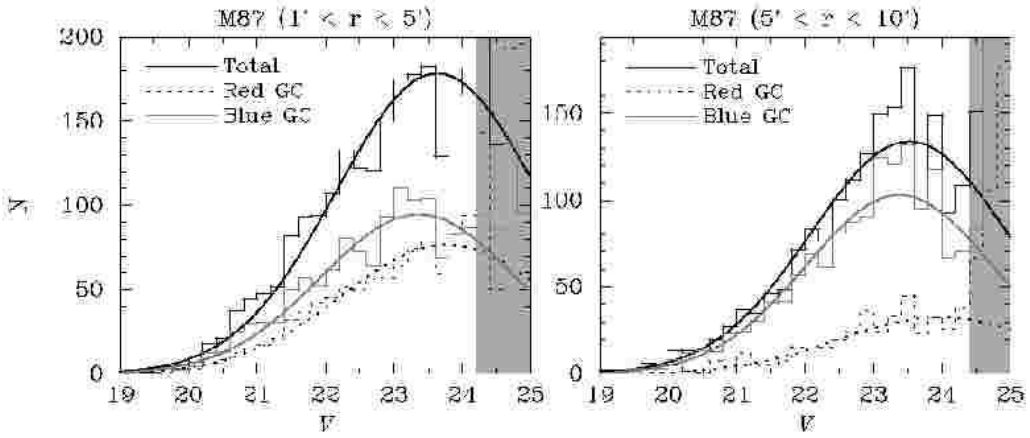

Figure 17. Same as Fig. 16, but the GCLFs in the region of $1' \leqslant R \leqslant 5'$ around M87 are compared with those in the region of $5' \leqslant R \leqslant 10'$.

GCs is not substantial enough especially in the outer region ($5' \leqslant R \leqslant 10'$). Nevertheless, the $V_{\rm TO}$ of the GCLF obtained at $1' \leqslant R \leqslant 10'$ is consistent with that in the core region obtained by Kundu & Whitmore (2001) using HST/WFPC2 who found $V_{\rm TO} = 23.47 \pm 0.14$ mag with a fixed value of $\sigma = 1.3$, again suggesting that the GCLF shape does not depend significantly on distance from the host galaxy.

4.2 GC Specific Frequency

Using the $V_{\rm TO}$ and σ of the Gaussians fitted to the GCLFs presented in Fig. 15, we can estimate the total number of GCs associated with M87 or NGC 4552 and calculate a GC specific frequency (S_N). We first integrate a GCLF obtained in an annulus ($1'$ width) centered on the host galaxy down to the magnitude where the completeness becomes 50 %. This number is then multiplied by a correction factor to include the fainter GCs based on the Gaussian GCLF. This calculation is repeated out to a certain distance from the galaxy centre. We note that it is ideal to fit a Gaussian to a GCLF obtained in each annulus but this is difficult in practice, especially at large distances because the number of GCs is not substantial and statistical errors are significant. We therefore use the fitted Gaussian in the inner region ($\leqslant 10'$) of M87 or NGC 4552 independently of the distance from the host galaxy. In order to estimate the number of GCs at distances smaller than $\leqslant 1'$, where the brightness of host galaxy halo light exceeds the linearity regime of the CCD, the radial profile of GC surface density outside the core region is fitted with a de Vaucouleurs law profile (see Paper II for details) and the fitted formula is extrapolated towards the galaxy centre. The estimated total number of M87 GCs is 12000 ± 800 within $25'$ from the galaxy centre (cf. 13200 ± 1500 by HHM). For NGC 4552, the total number of GCs is estimated to be 1400 ± 170 within $10'$. Note that the fraction of GCs at $R \leqslant 1'$ estimated from the extrapolation is 8.5 % for M87 GCs and 17 % for NGC 4552 GCs. If we adopt $M_V = -22.46$ mag as the V-band absolute magnitude of M87, which is also adopted by HHM (a difference in adopted distance modulus of 0.03 mag is corrected),

the S_N value of M87 is calculated to be 12.5 ± 0.8, which is only slightly smaller than 14.1 ± 1.6 obtained by HHM. The V-band luminosity of NGC 4552 is obtained from our data by fitting a de Vaucouleurs law to the V-band surface brightness profile and integrating it out to the same distance ($10'$); $M_V = -21.12$ mag. The S_N value of NGC 4552 is then estimated to be 5.0 ± 0.6.[4]

5 SUMMARY

We have performed a wide-field imaging survey of the globular cluster (GC) populations around M87 with Suprime-Cam on the 8.2m Subaru telescope. A $2^\circ \times 0.^\circ5$ (560 kpc $\times$ 140 kpc) field extending from M87 to the east was observed through the BVI filters. In addition to this unprecedented large survey area, our data analysis has been optimized to study the statistical properties of GCs as follows:

- GC candidates are isolated not only with an extended source cut but also with a colour cut, where only unresolved objects falling on a specific region of the $B-V$ and $V-I$ colour-colour diagram are accepted. The colour criterion is defined so as to include almost all the Galactic GCs and to avoid foreground stars and background galaxies. This is expected to efficiently isolate bona-fide GCs from other unresolved objects on our imaging data.
- In order to assess foreground and background contamination which needs to be statistically subtracted, we analyze the imaging data on the HDF-N field and the Lockman Hole field as control field data. These fields cover reasonably wide sky areas ($\sim 30' \times 30'$) and are compatible with the data of the M87 fields in terms of the filter set (BVI), limiting magnitudes, and image qualities. We therefore extract contaminating populations using identical criteria to those adopted in the M87 fields, minimizing the possibility of introducing any systematic errors into the subtractive correction.

In this paper, we have investigated the luminosity function and global specific frequency (S_N) of GC candidates surrounding M87 or NGC 4552. The V-band GC luminosity functions (GCLFs) were obtained in the inner regions of M87 and NGC 4552 at distances $\leqslant 10'$ from the galaxy centres. By fitting Gaussians to the GCLFs, the turnover magnitude is estimated to be 23.62 ± 0.06 mag for M87 GCs and 23.56 ± 0.20 mag for NGC 4552 GCs. The GCLF appears to depend on GC colour; the turnover magnitude in the GCLF of the red GC subpopulation ($V-I > 1.1$) is ~ 0.5 mag and 0.4 mag fainter than that of the blue GC subpopulation ($V-I \leqslant 1.1$) for the M87 GCs and NGC 4552 GCs, respectively.

For the M87 GCs, the GCLFs at $1' \leqslant R \leqslant 5'$ were compared with those at $5' \leqslant R \leqslant 10'$ but no obvious trend with radius was found in the shape of the GCLF for either the red or blue subpopulations. The global S_N of M87 GCs and NGC 4552 GCs is estimated to be 12.5 ± 0.8 within $25'$ and 5.0 ± 0.6 within $10'$, respectively.

[4] We calculated the total number of GCs and S_N within $10'$ for NGC 4552 to avoid possible contributions of M87 GCs and intergalactic GCs outside of this radius (see Paper II). If we fit a de Vaucouleurs law to the GC surface density profile within $10'$ from the NGC 4552 centre and integrate it out to $25'$ as done for M87 GCs, the number of GCs and S_N are estimated to be 2000 ± 660 and 6.2 ± 2.1, respectively.

ACKNOWLEDGEMENTS

We are grateful to the anonymous referee for careful reading of our manuscript and helpful comments. This work was based on data collected at Subaru Telescope and obtained from the SMOKA science archive at Astronomical Data Analysis Center, which are operated by the National Astronomical Observatory of Japan. We acknowledge the members of the Subaru telescope operation team, especially Dr. Hisanori Furusawa for supports during the observation. This work was partly supported by Grants-in-Aid for Scientific Research (Nos. 16540223 and 17540216) by the Japanese Ministry of Education, Culture, Sports, Science and Technology.

REFERENCES

Ashman, K. M., Conti, A., & Zepf, S. E. 1995, AJ, 110, 1164
Ashman, K. M., & Zepf, S. E. 1992, ApJ, 384, 50
Baba, H., et al. 2002, ADASS XI, eds. D. A. Bohlender, D. Durand, & T. H. Handley, ASP Conference Series, Vol. 281, 298
Barmby, P. 2003, in Extragalactic Globular Cluster Systems, ed. M. Kissler-Patig (New York, Springer), p. 143.
Bassino, L. P., Faifer, F. R., Forte, J. C., Dirsch, B., Richtler, T., Geisler, D., & Schuberth, Y. 2006, A&A, in press (astro-ph/0603349)
Beasley, M., Baugh, C. M., Forbes, D. A., Sharples, R. M., & Frenk, C. S. 2002, MNRAS, 333, 383
Bertin, E., & Arnouts, S. 1996, A&AS, 117, 393
Blakeslee, J. P. 1999, ApJ, 118, 1506
Brodie, J. P., Strader, J., Denicoló, G., Beasley, M. A., Cenarro, A. J., Larsen, S. S., Kuntschner, H., & Forbes, D. A. 2005, AJ, 129, 2643
Capak, P., et al. 2004, AJ, 127, 180
Cohen, J. G., & Ryzhov, A. 1997, ApJ, 486, 230
Cohen, J. G., Blakeslee, J. P., & Ryzhov, A. 1998, ApJ, 496, 808
Côté, P., Marzke, R. O., & West, M. J. 1998, ApJ, 501, 554
de Vaucouleurs, G., & Nieto, J. -L. 1978, ApJ, 220, 449
Dirsch, B., Richtler, T., Geisler, D., Forte, J. C., Bassino, L. P., & Gieren, W. P. 2003, AJ, 125, 1908
Elson, R. A. W., & Santiago, B. X. 1996, MNRAS, 280, 971
Fernández-Soto, A., Lanzetta, K. M., & Yahil, A. 1999, ApJ, 513, 34
Fioc, M., & Rocca-Volmerange, B. 1997, A&A, 326, 950
Forbes, D. A., Brodie, J. P., & Grillmair, C. J. 1997, AJ, 113, 1652
Forbes, D. A., et al. 2004, MNRAS, 355, 608
Gebhardt, K., & Kissler-Patig, M. 1999, AJ, 118, 1526
Geisler, D. 1996, AJ, 111, 480
Geisler, D., Lee, M. G., & Kim, E. 1996, AJ, 111, 1529
Hanes, D. A., Côté, P., Bridges, T. J., McLaughlin, D. E., Geisler, D., Harris, G. L. H., Hesser, J. E., & Lee, M. G. 2001, ApJ, 559, 812 (H01)

Harris, W. E. 1986, AJ, 91, 822
Harris, W. E. 1991, ARA&A, 29, 543
Harris, W. E. 1996, AJ, 112, 1487
Harris, W. E., Harris, G. L. H., & McLaughlin, D. E. 1998, AJ, 115, 1801 (HHM)
Jordán, A., Côté, P., West, M. J., & Marzke, R. O. 2002, ApJ *Letters*, 576, L113
Kissler-Patig, M., & Gebhardt, K. 1998, AJ, 116, 2237
Kundu, A., Whitmore, B. C., Sparks, W. B., Macchetto, D., Zepf, S. E., & Ashman, K. M. 1999, ApJ, 513, 733 (K99)
Kundu, A., & Whitmore, B. C. 2001, AJ, 121, 2950
Landolt, A. U. 1992, AJ, 104, 340
Larsen, S. S., Brodie, J. P., Huchra, J. P., Forbes, D. A., & Grillmair, C. J. 2001, AJ, 121, 2974 (L01)
McLaughlin, D. E. 1999, AJ, 117, 2398
McLaughlin, D. E., Harris, W. E., & Hanes, D. A. 1994, ApJ, 422, 486
Miyazaki, S., et al. 2002, PASJ, 54, 833
Moore, B., Diemand, J., Madau, P., Zemn M., & Stadel, J. 2005, MNRAS, submitted (astro-ph/0510370)
Ouchi, M., et al. 2004, ApJ, 611, 660
Peng, E. W., et al. 2005, ApJ, 639, 95
Pickles, A. 1998, PASP, 110, 863
Rhode, K. L., & Zepf, S. E. 2001, AJ, 121, 210
Rhode, K. L., & Zepf, S. E. 2004, AJ, 127, 302
Schlegel, D. J., Finkbeiner, D. P., & Davis, M. 1998, ApJ, 500, 525
Strader, J., Brodie, J. P., & Forbes, D. A. 2004, AJ, 127, 3431
Strader, J., Brodie, J. P., & Forbes, D. A. 2004, AJ, 127, 3431
Strader, J., Brodie, J. P., Spitler, L., & Beasley, M. A. 2005, AJ, submitted (astro-ph/0508001)
Strom, S. E., Forte, J., Harris, W., Strom, K. M., Wells, D., & Smith, M. 1981, ApJ, 245, 416
Tamura, N., Sharples, R. M., Arimoto, N., Onodera, M., Ohta, K., & Yamada, Y. 2006, MNRAS, submitted (Paper II)
Tonry, J. L., Dressler, A., Blakeslee, J. P., Ajhar, E. A., Fletcher, A. B., Luppino, G. A., Metzger, M. R., & Moore, C. B. 2001, ApJ, 546, 681
West, M. J. 1993, MNRAS, 265, 755
White, R. E. 1987, MNRAS, 227, 185
Yagi, M., Kashikawa, N., Sekiguchi, M., Doi, M., Yasuda, N., Shimasaku, K., Okamura, S. 2002, AJ, 123, 66